Chemical Engineering Journal 428 (2022) 131239

Contents lists available at ScienceDirect

Chemical Engineering Journal

journal homepage: www.elsevier.com/locate/cej

Assessing CH_4/N_2 separation potential of MOFs, COFs, IL/MOF, MOF/Polymer, and COF/Polymer composites

Hasan Can Gulbalkan [a], Zeynep Pinar Haslak [a], Cigdem Altintas [a], Alper Uzun [a,b,c], Seda Keskin [a,*]

[a] Department of Chemical and Biological Engineering, Koc University, Rumelifeneri Yolu Sariyer, 34450 Istanbul, Turkey
[b] Koç University TÜPRAŞ Energy Center (KUTEM), Koç University, Rumelifeneri Yolu 34450 Sariyer, Istanbul, Turkey
[c] Koç University Surface Science and Technology Center (KUYTAM), Koç University, Rumelifeneri Yolu 34450 Sariyer, Istanbul, Turkey

ARTICLE INFO

Keywords:
Metal organic framework (MOF)
Covalent organic framework (COF)
Ionic Liquid (IL)
Molecular simulations
Density functional theory (DFT)

ABSTRACT

Separating CH_4/N_2 mixture is challenging, and performance of the existing materials is still open to improvement. In this study, we examined both the adsorption- and membrane-based CH_4/N_2 separation performances of 5034 different materials, including metal organic frameworks (MOFs), covalent organic frameworks (COFs), ionic liquid (IL)/MOF composites, MOF/polymer composites, and COF/polymer composites by performing high-throughput computational screening and molecular simulations. The top performing adsorbents and membranes were identified by computing several performance evaluation metrics. Investigation of the interactions between the gas molecules, the IL, and the top MOF was performed by density functional theory (DFT) calculations. Results pointed out that the interactions between the gas molecules and the linker fragments of the MOF are stronger than their interactions with the IL. Thus, as the IL molecules are loaded into the selected top MOF, they occupy the adsorption sites of the gases, decreasing CH_4 and N_2 uptakes and increasing the CH_4/N_2 selectivity. Our results revealed that MOFs offer great potential for adsorption-based CH_4/N_2 separation, and IL incorporation into MOFs remarkably increases their CH_4/N_2 selectivities. More than 25% of MOF and 70% of the COF membranes surpassed Robeson's upper bound because of high N_2 permeabilities and outperformed conventional polymeric membranes. N_2 permeabilities and selectivities of MOF/polymer and COF/polymer composites were found to be significantly higher than those of pure polymers. Our results emphasize the promises of the design and development of new MOF and COF adsorbents, membranes, and their composites with ILs and polymers for efficient CH_4/N_2 separation.

1. Introduction

Metal organic frameworks (MOFs) have emerged as promising alternatives for adsorption- and membrane-based gas separations due to their wide ranges of pore sizes, high surface areas, and ease of structural modifications [1,2]. The unlimited number of possible combinations of various metals and organic linkers have led to the synthesis of a large variety of MOFs with the number of synthesized MOFs is exceeding 103,000 as of January 2021 [3]. Experimental examination of thousands of MOFs for various gas separations requires a significant amount of time and effort. Therefore, computational studies play a significant role in describing physical properties and predicting gas separation performances of thousands of materials. Many studies on high-throughput computational screening of MOFs focused on CO_2 separation, mainly CO_2/CH_4 [4,5], CO_2/N_2 [6], and CO_2/H_2 [7]. CH_4/N_2 separation, which is important for natural gas purification, is challenging since CH_4 and N_2 have similar kinetic diameters (3.80 Å and 3.64 Å, respectively) and polarizabilities [8]. As a result, low CH_4/N_2 selectivities have been reported when different types of porous adsorbents are used, such as zeolites (1.8–3.9) [9], zeolite molecular sieves (3.4) [10], mesoporous carbons (3.7) [11], and activated carbon beads (5.5) [12]. Therefore, examining the upper limits of MOFs for CH_4/N_2 separation and identifying the best materials offering high selectivity is crucial.

A few computational studies have focused on a small number of MOFs to compute CH_4/N_2 selectivities using Grand Canonical Monte Carlo (GCMC) simulations. Liu and Smit [13,14] used molecular simulations to compute CH_4/N_2 selectivities of three zeolites (5–14) and seven MOFs (2.5–5) for an equimolar CH_4/N_2 mixture up to 20 bar, at

* Corresponding author.
E-mail address: skeskin@ku.edu.tr (S. Keskin).

https://doi.org/10.1016/j.cej.2021.131239
Received 4 May 2021; Received in revised form 16 June 2021; Accepted 6 July 2021
Available online 12 July 2021
1385-8947/© 2021 The Author(s). Published by Elsevier B.V. This is an open access article under the CC BY-NC-ND license (http://creativecommons.org/licenses/by-nc-nd/4.0/).

298 K, and two zeolitic imidazolate frameworks (ZIFs), ZIF-68 (3.5) and ZIF-69 (3.2), up to 30 bar, at 298 K. Sumer and Keskin [15] calculated adsorption selectivities of 102 MOFs for CH_4/N_2 separation using molecular simulations and reported the selectivities of the top five adsorbents in the range of 5.9–7.2 and 4.6–5.7 for vacuum swing adsorption (VSA) and pressure swing adsorption (PSA), respectively. Yan et al. [16] investigated the correlations between adsorption energies of gases, porosities, and CH_4/N_2 selectivities of MOFs and showed that selectivities are positively correlated with the adsorption energy densities of gas molecules inside MOFs. Computational studies on membrane-based CH_4/N_2 separation performances of MOFs are very limited. Membrane-based N_2/CH_4 mixture separation was examined using molecular simulations for hypothetical [17] and real [18] MOFs, and results showed that the pore limiting diameter and the pore size distribution of materials are the essential parameters affecting the gas diffusion and permeation through MOF membranes.

Since CH_4/N_2 selectivities of MOFs are still open to improvement, alternative porous materials, such as covalent organic frameworks (COFs), and structural modifications, such as post-synthesis modification of MOFs by incorporating ionic liquids (ILs) into their pores, have been considered. Our group recently demonstrated that COFs have comparable CO_2/N_2 and CO_2/H_2 separation performances to many MOFs [19,20]. However, none of the large-scale computational screening studies focus on COFs as adsorbents and/or membranes for CH_4/N_2 separation to date. Generating IL/MOF composites is an alternative to enhance the separation performances of pristine MOFs. But synthesizing and testing every composite for a particular application is time-consuming. Therefore, molecular simulations are recently used to identify the promising IL/MOF composites. For instance, incorporation of an IL, 1-ethyl-3-methylimidazolium thiocyanate ([EMIM][SCN]), into MOFs resulted in two times higher CH_4/N_2 selectivities compared to pristine MOFs [21] and our group also reported improved CH_4/N_2 selectivities for different IL/MOF composites [22].

This brief literature review shows that we have very limited information on CH_4/N_2 separation performances of COFs, MOFs, and their IL-incorporated composites. To unlock their potentials, we performed a high-throughput computational screening study by combining GCMC and molecular dynamics (MD) simulations to examine both adsorption- and membrane-based CH_4/N_2 separation performances of 4738 MOFs and 296 COFs. Their CH_4/N_2 adsorption capacities were compared at both VSA and PSA conditions. The top adsorbents were identified by computing several performance metrics, adsorption selectivity, working capacity, adsorbent performance score, and regenerability. We then incorporated an IL, 1-*n*-butyl-3-methylimidazolium-thiocyanate [BMIM][SCN], into the selected top MOFs to generate IL/MOF composites and investigated their CH_4/N_2 separation performance. Molecular simulations were performed to study the effects of increasing IL loading on the selectivities of composites and the density functional theory (DFT) calculations were used to quantify the interactions of CH_4 and N_2 with one of the selected MOFs and IL. We finally conducted computationally expensive MD simulations to compute gas permeabilities of MOF and COF membranes in addition to MOF/polymer and COF/polymer composite membranes, where the top MOFs and COFs were used as filler particles in polymers. Structural properties of materials, such as pore sizes, surface areas, and porosities were computed to establish the structure-performance correlations, which will present guidelines for the synthesis of new COFs, MOFs, their composites with ILs and polymers to achieve outstanding CH_4/N_2 separation performances.

2. Computational details

2.1. MOFs and COFs

The most recent computation-ready experimental all solvents removed (CoRE MOF 2019 ASR) database was used in this work, which contains 10,143 non-disordered MOFs with pore limiting diameter (PLD) $>$ 2.4 Å [23]. The third version of the CoRE COF database, consisting of 309 COF structures, was also studied [24]. The atomic coordinates of HAT-NTBA-COF were corrected following the warning in the literature [25]. Structural properties of MOFs and COFs, such as pore limiting diameter (PLD), the largest cavity diameter (LCD), N_2 accessible surface area (S_{acc}), geometric pore volume, porosity (ϕ), and density (ρ) were computed using Zeo++ software [26]. MOFs and COFs with nonzero gravimetric surface areas and PLDs $>$ 3.8 Å were examined to ensure that both CH_4 (3.80 Å) and N_2 (3.64 Å) can transport through the pores of the adsorbents and membranes. In addition, MOFs with gas diffusivities $< 10^{-8}$ cm^2/s were excluded in the membrane analysis since this value is the lower limit for accurate diffusion characterization using the equilibrium MD simulations. After these eliminations, we ended up with 4738 MOF and 296 COF structures.

2.2. Adsorption simulations in MOFs and COFs

In our previous works [15,27], we demonstrated the validity of our computational method by comparing simulation results of CH_4 and N_2 with experimental adsorption data of MOFs. GCMC simulations were conducted using the RASPA [28] simulation code version 2.0.37 to obtain the gas uptakes in each MOF and COF. RASPA is an open-source code that can perform simulations for the adsorption and diffusion of molecules in various MC and MD ensembles, energy minimizations, and free energy calculations. The temperature was set to room temperature (298 K) for all simulations. The Lennard Jones (LJ) potential was used to define the van der Waals interactions between gas–gas and gas-material atoms. To obtain the potential parameters for van der Waals interactions of MOF and COF atoms, the Universal Force Field (UFF) was utilized [29]. CH_4 was modeled as a single-site molecule [30]. N_2 was modeled as a three-site rigid molecule with N atoms at the two sites, and the third site was the center of mass with partial charges [31]. Potential parameters of gas models considered in this study are given in Supporting Information (SI) as Table S1. The Lorentz-Berthelot mixing rules were implemented to obtain pair potentials between different atoms. Electrostatic interactions were considered for N_2 molecules in addition to van der Waals interactions. As implemented in RASPA, the charge equilibration (Qeq) method was utilized to assign partial charges to MOF atoms to calculate electrostatic interactions between N_2 molecules and MOF atoms [32,33]. Long-range electrostatic interactions were considered using the Ewald summation [34].

The Widom particle insertion method was used to calculate Henry's constants (K°) of CH_4 and N_2, and the simulations at infinite dilution were performed with 50,000 initialization cycles and a total number of 10^5 cycles. We then performed GCMC simulations for equimolar CH_4/N_2 mixture at three different pressures, 0.1, 1, and 10 bar at 298 K to consider both VSA and PSA conditions. Adsorption (desorption) pressures were set to 1 (0.1) and 10 (1) bar for VSA and PSA conditions, respectively. GCMC simulations for CH_4/N_2 mixture were performed with 60,000 cycles (10,000 cycles for initialization, 50,000 cycles for taking ensemble averages). The cut-off distance was set to 13 Å, and the simulation cell lengths were expanded to at least 26 Å. GCMC results were used to calculate various metrics, namely, selectivity ($S^0_{ads,\ CH_4/N_2}$ and $S^{mix}_{ads,\ CH_4/N_2}$), working capacity (ΔN_{CH_4}), regenerability (R%), and adsorbent performance score (APS) of MOFs as shown in Table S2. Ideal selectivity was defined as the ratio of the amount of the strongly adsorbed component (CH_4) to the amount of the weakly adsorbed component (N_2), while mixture selectivity was computed as the ratio of the composition of the adsorbed gases divided by the bulk composition of the mixture. Working capacity was calculated by subtracting the CH_4 uptake computed at the desorption pressure from the one computed at the adsorption pressure. The adsorbent performance score was calculated by multiplying the selectivity and working capacity. Regenerability was obtained by dividing the working capacity to the gas uptake

at the adsorption pressure. The values of isosteric heat of adsorption for CH_4 (Q_{st,CH_4}) were obtained from the mixture GCMC simulations conducted at 0.1 bar and 1 bar [35].

Adsorption Simulations in IL/MOF Composites: In a previous report, we experimentally showed that incorporating [BMIM][SCN] into ZIF-8 significantly improved CO_2/N_2 and CO_2/CH_4 selectivities [36]. In this work, [BMIM][SCN] was incorporated into the top three MOFs to examine the separation performances of IL/MOF composites for CH_4/N_2 mixture. Several of our previous studies showed the good agreement between the experimentally measured CO_2, CH_4, and N_2 uptakes of [BMIM][PF_6]/ZIF-8 [37], [BMIM][BF_4]/ZIF-8 [38], [BMIM][BF_4]/CuBTC [22], and [BMIM][BF_4]/UiO-66 [39] and results of GCMC simulations where we used rigid IL structures. Motivated from these good agreements shown for different gases, ILs and MOFs, we did not consider the flexibility of IL in simulations. Optimization of ILs and minimization procedures for IL/MOF composites were implemented as described in our previous work [22]. At least 3 and at most 27 IL molecules corresponding to 2–15 wt% loading were incorporated into MOFs. The upper limit for IL loading was set to 15 wt% since the incipient wetness limit of MOFs in experiments was generally between 15 and 30 wt% [40,41]. GCMC simulations for the adsorption of equimolar CH_4/N_2 mixture in IL/MOF composites were performed at 1 bar, 298 K. The force field and the number of cycles were the same as described above.

2.3. Density functional theory (DFT) calculations

The quantitative analysis of CH_4 and N_2 interactions with one of the top MOFs and the IL was performed using DFT calculations. All possible conformations of the molecules were located with Becke-three-parameter-Lee-Yang-Parr (B3LYP) [42,43] functional, including Grimme's D2 correction [44] using the Gaussian09 program package. All electron 6-31G* basis set was defined for all atoms except metal center for which LANL2DZ was used. The vibrational frequency analysis was implemented to ensure no imaginary frequency remained. Natural bond orbital (NBO) atomic charges and binding energies were further calculated with 6–311++G** basis set by performing single point calculations on the optimized geometries. Energies obtained from single point calculations are corrected with zero-point corrections. The binding energies between the adsorbed gases and the IL or MOF are computed by using $\Delta E_{bind} = E_{A+B} - (E_A + E_B) + \delta^{BSSE}$ where E_{A+B} is the energy of the system consisting of the adsorbed gas molecule (CH_4 or N_2) and the adsorbent (IL or MOF), E_A is the energy of the adsorbent (IL or MOF), and E_B is the energy of the gas molecule, and δ^{BSSE} is the basis set superposition error correction employed by Counter Poise approach.

2.4. Diffusion simulations in MOFs and COFs

The validity of our computational method to predict the performances of MOF membranes was presented in our previous works [6,45]. The self-diffusion coefficients (D^0) of CH_4 and N_2 gases were computed performing MD simulations at infinite dilution. Thirty adsorbate molecules were placed into each MOF and COF, and gas–gas interactions were switched off to mimic infinite dilution. MD simulations were carried out for a total of 4×10^6 cycles in addition to 20,000 initialization and 10,000 equilibration cycles using the NVT ensemble with the Nose-Hoover thermostat [46]. Self-diffusion coefficients were computed from the mean squared displacement of the gases [47]. As shown in Table S2, K^0 and D^0 values were used to calculate adsorption, diffusion, membrane selectivity (S^0_{mem}), and gas permeability (P^0).

Membrane Calculations for MOF/Polymer Composites: We finally examined N_2/CH_4 separation performances of MOF/polymer and COF/polymer membranes. These composites are mixed matrix membranes (MMMs) where the MOFs or COFs are incorporated into a polymer to improve the gas separation potential of the pure polymer. The top five MOFs, UTEWOG [48], HUYJUG [49], OQANIE [50], JOGHIY [51], VONCOS [52], and five COFs, ICOF-2 [53], COF-DL229-7fold [54], COF-42-gra [55], OH-TAPH-COF [56], and COF-DL229 [54] were used as fillers and five different types of polymers were used for MMMs. Polymers that are close to the Robeson's upper bound [57], 6FDA-TAB poly (pyrrolone) [58], copolymer of tetrafluoroethylene (TFE) and 2,2,4-trifluoro-5-trifluoromethoxy-1,3-dioxole (TTD) (Hyflon AD60X) [59], poly (trimethylsilyl-propyne-co-phenylpropyne) (PTMSPcoPP) [60], poly (trimethylsilyl-propyne) (PTMSP) [61], and poly(2,2-bis (trifluoromethyl)-4,5-difluoro-1,3-dioxole-co-tetrafluoroethylene (Teflon AF2400) [62] were selected. Experimentally reported N_2, CH_4 permeabilities, and N_2/CH_4 selectivities of the polymers were obtained from the literature and presented in Table S3. Gas permeabilities of MMMs (P_{MMM}) were computed by the Maxwell model [63], which uses the gas permeability data of polymers (P_P) given in the literature and gas permeability of MOFs (P^0) computed in this work, as shown in Table S2. The geometry shape factor (n) was taken as 0.3 assuming sphere-like MOF and COF particles [64], and the filler volume fraction (ϕ) in the polymer matrix was taken as 0.2. This computational approach to predict the gas permeabilities of MOF/polymer composites has been validated by comparing the simulation results with the available experimental data in previous works [65,66].

3. Results and discussion

3.1. Adsorption-based separation of CH_4/N_2

We computed both the ideal (S^0_{ads}) and equimolar CH_4/N_2 mixture selectivities ($S_{ads,\,mix}$) to compare separation performances of MOFs and COFs at different conditions. S^0_{ads} values were computed at infinite dilution and $S_{ads,\,mix}$ values were computed at 1 and 10 bar using the results of binary mixture GCMC simulations. Fig. S1 compares S^0_{ads} and $S_{ads,\,mix}$ of 4738 MOFs and 296 COFs. All MOFs are CH_4 selective except for five of them, whereas all COFs are CH_4 selective. The reason is that dispersion forces have an important effect when nonpolar molecules are strongly trapped inside the narrow pores [67]. CH_4 has a higher energetic interaction parameter ($\varepsilon/k_B = 148.0$ K) than N_2 ($\varepsilon/k_B = 36.4$ K), leading to higher host-adsorbate potential energies for CH_4. The deviation between S^0_{ads} and $S_{ads,\,mix}$ increases with pressure for both MOFs and COFs since most adsorption sites are filled with gas molecules at high pressures, and gases compete more for the remaining adsorption sites. S^0_{ads} of many MOFs and COFs are higher compared to their $S_{ads,\,mix}$ especially at high pressures, due to the availability of all adsorption sites to both gases at infinite dilution. $S_{ads,\,mix}$of COFs (1.1–7.6 and 1.1–10.3) are generally lower compared to MOFs (0.8–14.7 and 0.9–14.1) at 1 and 10 bar, respectively. The deviation of S^0_{ads} and $S_{ads,\,mix}$ is higher when S^0_{ads} is high for most of the MOFs and COFs. These results show that MOFs can provide more attractive adsorption sites to gas molecules than COFs, and the selectivities of the former are more affected by the competition of gas molecules at mixture conditions. Therefore, considering the mixture selectivity of MOFs is important for evaluating their CH_4/N_2 mixture separation performances.

Considering working capacity, ΔN_{CH_4}, together with $S_{ads,\,mix}$ provides a more realistic view of CH_4/N_2 separation performances of materials since these metrics give an idea for the productivity of the adsorption unit and the purity of the end product. There is a trade-off between these two metrics, which was observed in various gas separations [68,69]. Therefore, for an efficient separation process, both high $S_{ads,\,mix}$ and high ΔN_{CH_4} leading to high APS is required. We colour-coded the MOFs and COFs according to their APSs in Fig. 1. At VSA condition, the range of ΔN_{CH_4}, $S_{ads,\,mix}$, and APS of MOFs are 0.01–2.7 mol/kg, 0.8–14.7, 0.02–33.8 mol/kg, respectively, while for COFs lower values were predicted (0.07–2 mol/kg, 1.1–7.6, 0.15–15 mol/kg) as shown in Fig. 1(a). MOFs with $S_{ads,\,mix} > 6$ and $\Delta N_{CH_4} > 1$ mol/kg generally have moderate and high APSs, while the highest APSs (20–34

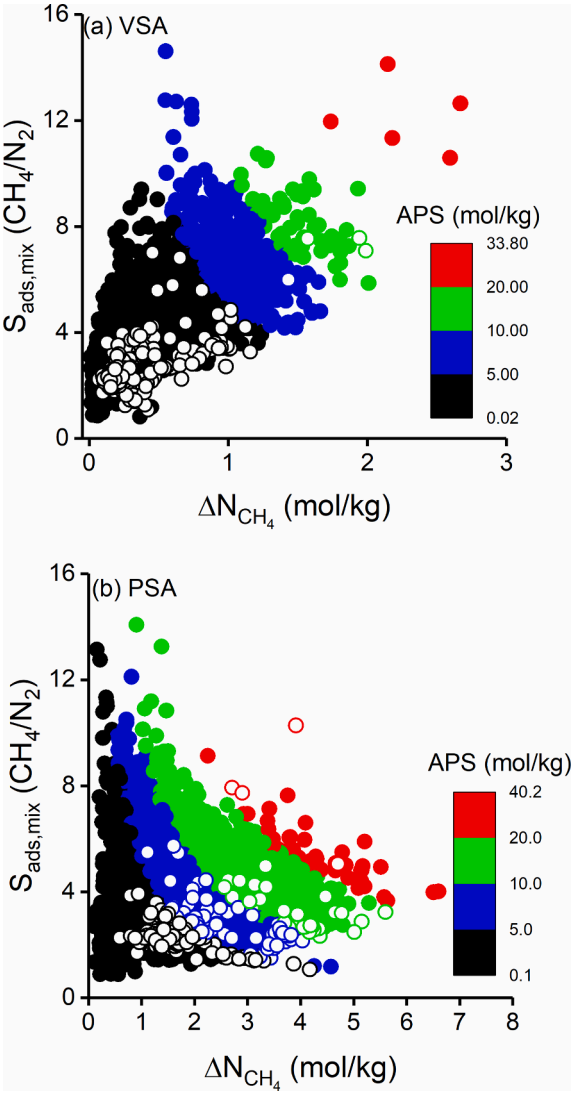


Fig. 1. The relationship between $S_{ads,\ mix}$ and ΔN_{CH_4} of MOFs and COFs at (a) VSA, (b) PSA conditions. Filled (empty) circles represent MOFs (COFs), coloured according to the range of APS.

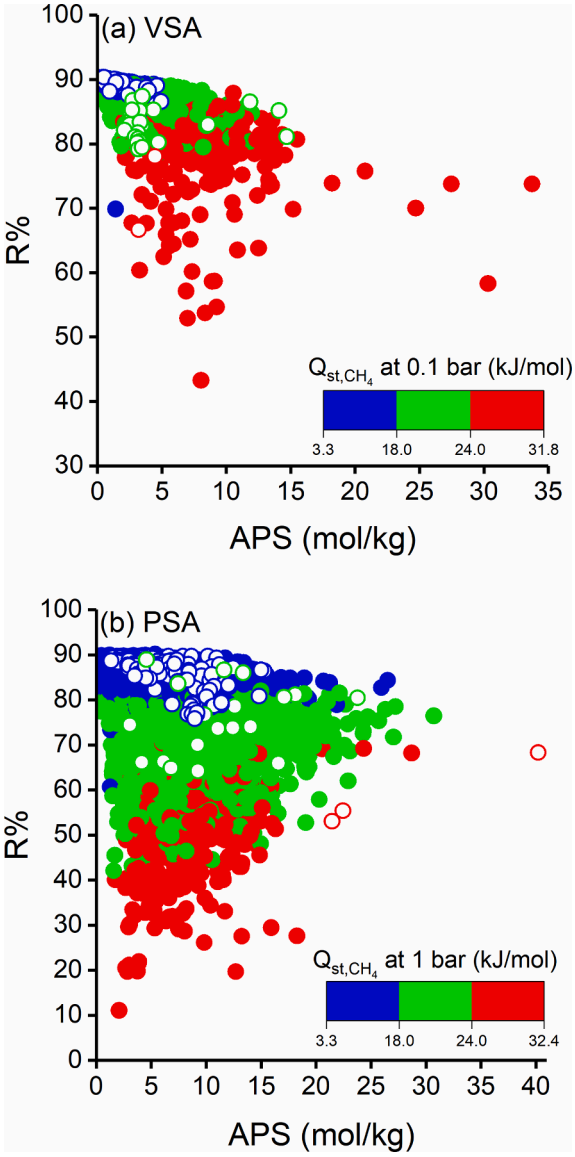


Fig. 2. The relationship between R% and APS of MOFs and COFs at (a) VSA, (b) PSA conditions. Filled (empty) circles represent MOFs (COFs), coloured according to the range of Q_{st,CH_4} at the desorption condition.

mol/kg) are observed for MOFs with $\Delta N_{CH_4} > 2$ mol/kg and $S_{ads,\ mix} > 10$. Most of the COFs have $S_{ads,\ mix} < 8$ and $\Delta N_{CH_4} < 1$ mol/kg, leading to APSs not higher than 5 mol/kg. Conversely to VSA condition, a trade-off between ΔN_{CH_4} and $S_{ads,\ mix}$ is observed at PSA condition, especially for MOFs, as shown in Fig. 1(b). MOFs with high $S_{ads,\ mix}$ at this condition have less available space and cannot provide high ΔN_{CH_4}. Still, higher ΔN_{CH_4} are obtained at this condition compared to VSA. Data showed that there are more MOFs and COFs with APS > 10 mol/kg at PSA, and the APSs of some COFs can even surpass those of some MOFs. APS values of 4 COFs are considerably higher than the APS values of MOFs at PSA condition. For example, the APS of NPN-3 [70] is 40.2 mol/kg, while the highest APS obtained with MOFs is 30.7 mol/kg at PSA condition. The APSs of TPE-COF-I [71] (23.8 mol/kg), NPN-2 [70] (22.4 mol/kg), and NPN-1 [70] (21.5 mol/kg) surpass the APSs of 99% of MOFs. We note that the NPN-series have narrow pore sizes between 5.3 and 6.1 Å and additional surfaces for adsorption due to the interpenetration of frameworks [72], which enhanced the working capacity, selectivity, and ultimately APS of these COFs.

Adsorption-based gas separation generally requires cyclic usage of the adsorbent. Thus, R% is essential in determining the most promising materials [73]. In Fig. 2, we compared R% and APS at VSA and PSA conditions for MOFs and COFs. As shown in Fig. 2(a), materials with high APS generally suffer from low R% at VSA condition, and the colour code indicates that most of these materials have $Q_{st,CH_4} > 18$ kJ/mol at 0.1 bar. For the materials with high Q_{st,CH_4} at 0.1 bar, the interaction of gases with the adsorbent is strong, which leads to high CH_4 uptake at adsorption pressure but a low number of desorbed molecules at desorption pressure. We also observed that for most of the COFs, the Q_{st,CH_4} values are lower than those of MOFs. At PSA condition, many MOFs and COFs having APS > 15 mol/kg can also provide a sufficient R % > 70% and a high range of Q_{st,CH_4} values (16–24 kJ/mol).

Next, we identified the top 20 MOF and COF adsorbents for CH_4/N_2 separation, considering materials with the highest APS for VSA and PSA processes in addition to R% > 80%. Selectivities and main structural features of these top materials are provided in Tables S4-S5. 18 (15) of the top 20 MOFs were found to have LCDs < 6.1 (8.1) Å for the VSA (PSA) process, which indicates that promising materials have narrow pores that capture CH_4 selectively. One main outcome from Table S4 is that the top MOFs have either heterocyclic linkers containing at least one nitrogen and/or carbocyclic linkers. A DFT study reported that cyclic linkers increase the number of binding sites for CH_4 adsorption and

the presence of heterocyclic linkers is more effective in CH_4 adsorption than the carbocyclic linkers at low pressures [74]. These results are consistent with our findings since all the top MOFs at VSA condition have heterocyclic linkers containing at least one nitrogen. Similarly, the results of a combined experimental and simulation study for CH_4/N_2 mixture showed that the existence of cyclic linkers positively influences CH_4 adsorption [75]. SAHYAD03 [76] and VAZROF [77] are among the representative MOFs with high selectivity (9.3 and 8.6, respectively) containing both heterocyclic and carbocyclic linkers, and MUHNUA [78] is a representative material with high selectivity (8.7) containing heterocyclic pyrazole linkers. At PSA condition, half of the top MOFs have carbocyclic linkers, consisting of benzene or phenyl, and the other half have heterocyclic linkers. In most cases, COFs have larger pore sizes than MOFs, and both CH_4 and N_2 can be adsorbed into the pores, which indicates that pore size is not a key factor for promising COFs. Table S5 shows that the top 20 COFs have LCDs in the range of 5.3–27.0 Å (6.1–25.7 Å) for the VSA (PSA) process. The structures of the selected top 3 MOFs and COFs for PSA condition are given in Table S6. Fig. S2(a and b) represents the relation between porosity, LCD/PLD, and $S_{ads,\ mix}$ for MOFs at 1 and 10 bar. MOFs with $S_{ads,\ mix} > 9$ at 1 and 10 bar have narrow LCD/PLD ratios (1–1.6) and the same range of porosities (0.34–0.53). The trend indicates that the highest selectivities are obtained when the cavities and the channels are similar in size. As shown in Fig. S2(c and d), COFs with $S_{ads,\ mix} > 5$ at 1 and 10 bar have narrow LCD/PLD ratios (1–1.3) similar to MOFs, but they have a larger range of porosities (0.44–0.72).

We next investigated IL/MOF composites for CH_4/N_2 separation. [BMIM][SCN] was incorporated into the selected top three MOFs, SAHYAD03, VAZROF, and MUHNUA, to examine the effect of IL on their selectivities. The structures of the IL/MOF composites are given in Table S6. Fig. 3(a) shows the number of adsorbed CH_4 and N_2 per unit cell of each MOF with respect to the increasing number of ILs incorporated into the MOFs. The trend indicates that the number of available adsorption sites for CH_4 and N_2 decreases upon IL incorporation. Fig. 3 **(b)** shows the change in adsorption selectivity at 1 bar with respect to the number of ILs and corresponding IL loadings in wt.% for the selected top MOFs. Although both the CH_4 and N_2 uptakes decreased because the increasing number of ILs reduces the available space in the pores, the decrease in N_2 uptakes was more pronounced compared to CH_4, which is due to the existence of heterocyclic imidazolium rings in the $[BMIM]^+$ cation that favors CH_4 over N_2. Therefore, CH_4/N_2 selectivities improved from 9.3 to 11.7, 8.6 to 10.2, and 8.7 to 9.5 for SAHYAD03, VAZROF, and MUHNUA loaded with 15, 12, and 9 wt% IL, respectively. Moreover, the corresponding selectivities improved with the increasing number of ILs inside these MOFs, which corresponds to higher IL loadings, up to 15 wt%, in the composite. These results were consistent with our previous experimental studies [37,38], which reported significant selectivity improvements as a function of increasing IL loading. We also compared the performances of the top performing MOFs having similar pore sizes with the pore sizes of the IL/MOF composites. For instance, the PLD of [BMIM][SCN]/MUHNUA is 3.8 Å, and it has a selectivity of 9.5 as previously mentioned. Most of the top MOFs at VSA condition have comparable pore sizes (3.8–5.1 Å) to that of [BMIM][SCN]/MUHNUA and their selectivities range from 5.9 to 9.3, indicating that the selectivity of the IL-incorporated composite is higher than all top MOFs except FIPWOS. We also note that the selectivity of a material does not only depend on the pore size, but it is a result of the complex interplay of many different physical and chemical properties such as pore size, pore functionality, metal type, charge distribution, topology etc. It is important to compare the adsorption-based separation performances of MOFs, COFs, and IL/MOFs with other high-performing adsorbents. The equimolar CH_4/N_2 selectivities of Cu-MOF [79], ATC-Cu [80], SBMOF-1 [81], Co-MOF [82], and Al-CDC [83] at 1 bar and 298 K were reported as 6.9, 9.7, 11.5, 12.5, and 13.1, respectively. The calculated selectivities in this work are in between 3.3 and 7.6, 5.9–9.8,

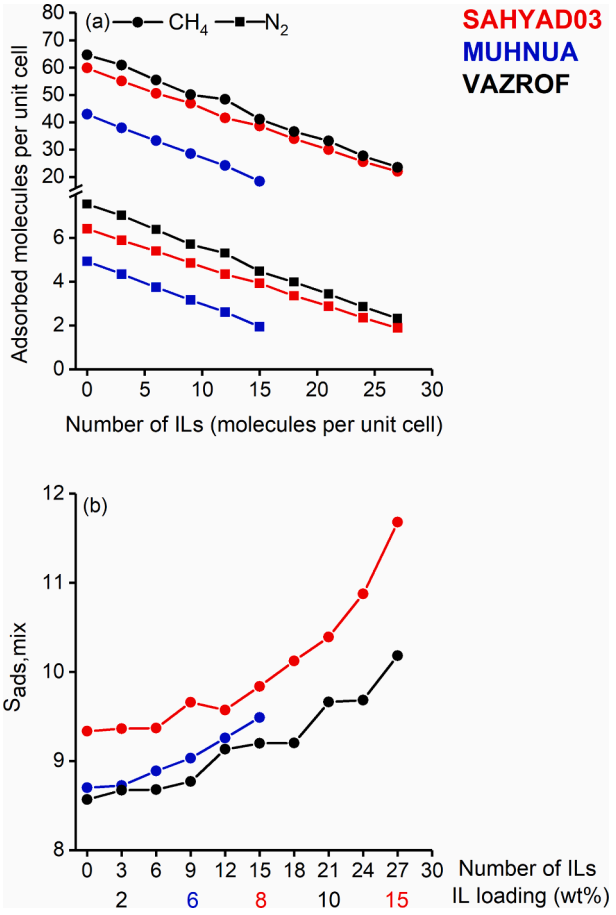


Fig. 3. The relationship between (a) adsorbed CH_4 and N_2 molecules per unit cell, (b) $S_{ads,\ mix}$, with respect to the number of IL molecules per unit cell and IL loading (wt%). Colours represented on the x-axis correspond with the MOF refcodes.

and 9.5–11.7 for the top COFs, MOFs, and IL/MOF composites, respectively, demonstrating that incorporating ILs into MOFs to generate IL/MOF composites offers a great potential for improving CH_4/N_2 selectivities of pristine MOFs.

Interactions between the gas molecules, the IL, and one of the top MOFs, SAHYAD03, were further investigated by performing DFT calculations. This approach was already shown to be successful in explainingthe interactions between CO_2-ZIF-8 and CO_2-ILs [84]. Two different cluster models were generated representing the adsorption sites to reduce the computational costs. The first cluster model contains the metal center (Cd) and four pyridine rings coordinated to Cd by their N atoms and two 3,5-diphenyl-4H-1,2,4-triazole-4-amine substituents coordinated by their N atoms on the heterocyclic ring. The second model was constructed from the linker fragments, which is 3,5-bis(3-(pyridine-4-yl)phenyl)-4H-1,2,4-triazole 4-amine, as shown in Fig. S3(a). To mimic the MOF's constrained environment, selected key atoms in cluster models are kept frozen, and the rest of the atoms are allowed to be fully optimized, as presented in Fig. S3(b and c). Optimization of CH_4 and N_2 in the first cluster model indicated that the Cd atom is not the primary adsorption site for these gases. Fig. S4 demonstrates that CH_4 and N_2 gases interact with the aromatic pyridine linker fragments and stabilize at the distances of 4.75 Å and 5.17 Å from the Cd atom, respectively.

To further investigate the interactions of gases with the linker atoms, another cluster model composed of only linker fragment was optimized in the presence of CH_4 and N_2. As there are three different rings in the fragment, the initial positions of the gases were placed in close proximity to the central triazole ring, phenyl and pyridine rings. According to the

DFT optimized geometries, the central triazole ring is the primary adsorption site for both gases since there are more interaction sites than the other rings. H3 of CH_4 molecule ($q_{H3} = 0.214e$) forms H-bonds with electron-rich nitrogen atoms (q_{N1} = -0.289e, q_{N2} = -0.310e) on the triazole ring, as shown in Fig. 4(a). Non-covalent interactions formed by H1 ($q_{H1} = 0.188e$) and H2 ($q_{H2} = 0.203e$) atoms with π-electron-rich aromatic phenyl rings stabilize CH_4 with a binding energy of 10.7 kJ/mol. On the other hand, N_2 slightly polarizes such that negatively charged N3 atom (q_{N3} = -0.039e) forms a hydrogen bond with H4 of amine ($q_{H4} = 0.367e$) and H5 of pyridine ring ($q_{H5} = 0.218e$) as shown in Fig. 4(b), and the slightly positive N4 atom ($q_{N4} = 0.043e$) interacts non-covalently with the negatively charged N2 atom on the triazole ring ($q_{N2} = -0.312e$) with a binding energy of 9.9 kJ/mol. As can be seen from Fig. 4(c), CH_4 is stabilized by a H-bond formed between H1 ($q_{H1} = 0.204e$) and N5 of triazole amine (q_{N5} = -0.616e) and the non-covalent H2···π interactions ($q_{H2} = 0.206e$) formed with the pyridine ring. These interactions stabilize the CH_4-linker fragment system by 8.3 kJ/mol. N_2 binds weaker than CH_4 with an energy of 6.1 kJ/mol. There is a weak H-bond between N3 ($q_{N3} = -0.007e$) and H6 ($q_{H6} = 0.209e$) and non-covalent interaction between N4 ($q_{N4} = 0.009e$) and C1 ($q_{C1} = -0.023e$) as represented in Fig. 4(d).

GCMC simulations revealed that upon incorporating [BMIM][SCN] into the selected top three MOFs, CH_4 and N_2 uptakes decrease, but the selectivity of CH_4 over N_2 increases. The dynamics of this behavior of gases were investigated by DFT calculations by optimizing the IL in the presence of the adsorbate molecules. The most stable conformer of [BMIM][SCN] is illustrated in Fig. 4(e) in which the non-bonded pairs on the nitrogen atom of the anion form intermolecular hydrogen bonds and non-covalent interactions with the cation. The optimization of [BMIM][SCN] with CH_4 and N_2 molecules showed that both gases interact differently with the IL molecule. CH_4 makes close contact with both the anion and the cation of the IL forming three hydrogen bonds with N atoms of the [BMIM] and [SCN] as shown in Fig. 4(f). On the other hand, one of the N atoms of slightly polarized N_2 molecule interacts non-

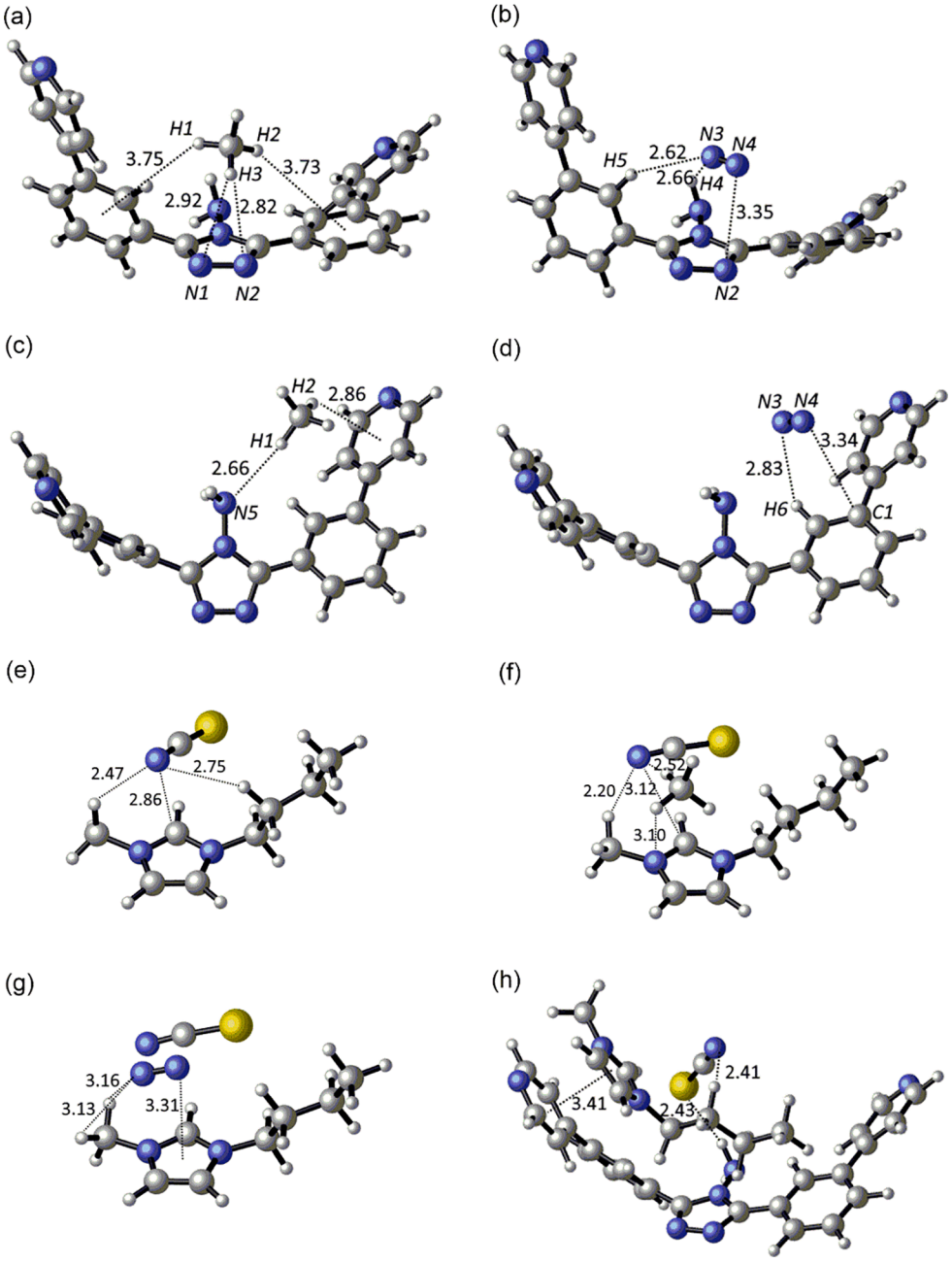


Fig. 4. 3D representations of the (a), (c) linker fragments in the presence of a CH_4 molecule, (b), (d) linker fragments in the presence of a N_2 molecule, (e) [BMIM][SCN], (f) [BMIM][SCN] in the presence of a CH_4 molecule, (g) [BMIM][SCN] in the presence of a N_2 molecule (h) [BMIM][SCN] in the presence of the linker fragment calculated at the B3LYP-D2/6-31G* level of theory. Bond distances are given in Å. Grey, white, yellow, and blue spheres represent C, H, S, and N atoms, respectively. Cartesian coordinates corresponding to these models are given in Table S9. (For interpretation of the references to colour in this Fig. legend, the reader is referred to the web version of this article.)

covalently with the π-electron-rich heterocycle of the cation while the other N atom forms two weak hydrogen bonds with the methyl substituent attached to [BMIM] as represented in Fig. 4(g). CH_4 shows a higher affinity towards [BMIM][SCN] with the calculated binding energy of 6.6 kJ/mol due to the stabilizing interactions between the gas and the IL, whereas N_2 has a lower affinity towards the IL molecules with the calculated binding energy of 2.4 kJ/mol.

According to the calculated binding energies, CH_4 and N_2 molecules bind stronger to the linker fragments of the MOF than they bind to the IL. As the ILs are loaded into the MOF, IL molecules occupy the adsorption sites (linker fragments) of the gases and act as new adsorption sites for CH_4 and N_2 molecules. Fig. 4(h) illustrates the optimized geometry of the linker fragment in the presence of [BMIM][SCN] in which the heterocyclic ring of the cation of the IL makes strong π-π stacking interactions with the pyridine ring present on the linker fragment. This interaction together with the H-bond between the S atom of the anion and the linker stabilizes the IL/MOF structure by 82.2 kJ/mol, which is 7.7- and 8.3-times stronger than the binding energies of CH_4 and N_2 gases with the linker fragment. In accordance with the GCMC simulations, the higher affinity of [BMIM][SCN] towards the SAHYAD03 structure shows that MOF prefers to bind to IL molecules rather than binding to CH_4 and N_2 gases.

3.2. Membrane-based separation of CH_4/N_2

We examined the diffusivity of N_2 and CH_4 inside MOFs and COFs in Fig. 5(a), which shows that $D^0_{N_2}$ is generally higher than $D^0_{CH_4}$. Since CH_4 has a lower molecular weight than N_2, it is expected to diffuse faster, but in most cases, stronger adsorption of CH_4 results in slower diffusion. Therefore, 3208 of the MOFs and 224 of the COFs have diffusion selectivities favouring N_2. In several applications involving gas mixtures, strongly adsorbed molecules have high adsorption selectivities, which results in low diffusion selectivities. However, for CH_4/N_2 separation, Fig. 5(b and c) shows that for 1526 MOFs and 72 COFs, both adsorption and diffusion can favour CH_4, which results in promising $S^0_{mem,\ CH_4/N_2}$ up to 47.4 for MOFs and 10.1 for COFs, respectively. Table S7 represents the $S^0_{mem,\ CH_4/N_2}$ and structural properties of the top five MOF and COF membranes for CH_4/N_2 separation. The top MOFs (COFs) have LCDs < 5.4 (15.8 Å) and porosities < 0.54 (0.69).

Polymers have been widely used to separate various gas mixtures, but they have a trade-off between selectivity and permeability, limiting their performance [85]. Since most of the polymers are N_2 selective, the data were presented with respect to $S^0_{mem,\ N_2/CH_4}$. Identification of the promising MOF and COF membranes that can overcome the trade-off for N_2/CH_4 separation is important. Fig. 6 represents $S^0_{mem,\ N_2/CH_4}$ as a function of N_2 permeability ($P^0_{N_2}$) together with Robeson's upper bound [57] to compare the separation performances of MOF and COF membranes with traditional polymeric membranes. Calculated $P^0_{N_2}$ values of MOFs (COFs) range from 2.9×10^3 to 1.3×10^7 (3.7×10^4–2.4×10^6) Barrer, which are higher than $P^0_{N_2}$ of polymers that range from 0.3 to 9.3×10^4 Barrer. Many MOFs and COFs surpass the upper bound owing to their high permeabilities, high selectivities, or both, indicating that both MOF and COF membranes have the potential to replace polymeric membranes for N_2/CH_4 separation. The top performing MOF and COF

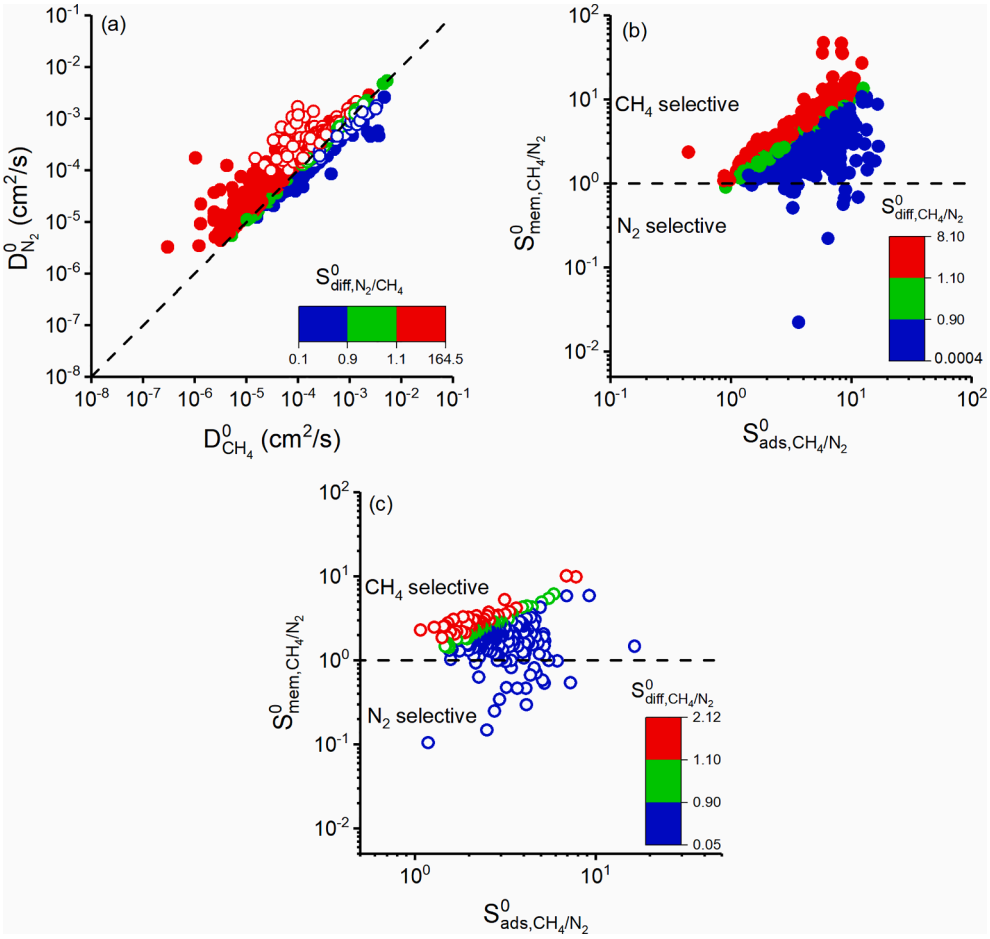


Fig. 5. (a) Comparison of $D^0_{CH_4}$ and $D^0_{N_2}$ in MOFs and COFs colour coded according to $S^0_{diff,\ N_2/CH_4}$. Relation of $S^0_{ads,\ CH_4/N_2}$ and $S^0_{mem,\ CH_4/N_2}$ in (b) MOFs, (c) COFs colour coded according to $S^0_{diff,\ CH_4/N_2}$. Filled (empty) circles represent MOFs (COFs).

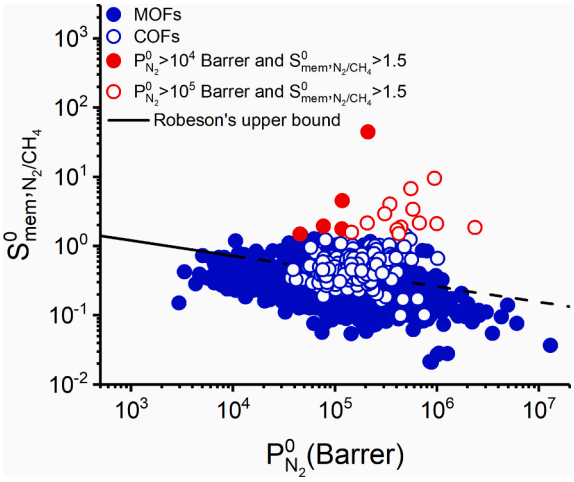


Fig. 6. $S^0_{mem,\ N_2/CH_4}$ and $P^0_{N_2}$ of MOF and COF membranes computed at infinite dilution. The black solid line represents Robeson's upper bound for N_2/CH_4 separation. The dashed line shows the predicted extension of Robeson's upper bound at high N_2 permeabilities. Filled (empty) circles represent MOFs (COFs).

membranes with $P^0_{N_2} > 10^4$ and $P^0_{N_2} > 10^5$ Barrer with $S^0_{mem,\ N_2/CH_4} > 1.5$ were shown with red in Fig. 6. 20 (21) of the MOF (COF) membranes were found to be N_2 selective over CH_4. Adsorption, diffusion, and membrane selectivities together with N_2 permeabilities and structural properties of the top five MOFs and COFs for N_2/CH_4 separation are presented in Table S8. The most promising MOF and COF membranes have LCDs (porosities) between 4.7 and 14.6 Å (0.55–0.70) and 6.1–17.2 Å (0.66–0.83), respectively. It is important to compare the membrane-based performances of MOFs with other types of membranes. N_2 permeability and N_2/CH_4 ideal selectivity were reported as 5.6 Barrer and 8.3 Barrer, respectively, for a carbon molecular sieve membrane at 4.5 bar and 298 K [86]. SAPO-34 zeolite membranes were reported to have N_2 permeabilities up to 3×10^3 Barrer and N_2/CH_4 selectivities between 9 and 11.2 [87]. An AlPO-18 membrane was reported to have a N_2 permeability and N_2/CH_4 selectivity as 7.7×10^3 Barrer and 3.8, respectively, at 298 K [88]. Recently, N_2 permeability and ideal N_2/CH_4 selectivity were reported as 1.3×10^3 Barrer and 24, respectively, for SSZ-13 zeolite membrane at 298 K [89]. These comparisons demonstrate that MOFs and COFs have much higher N_2 permeabilities and either comparable or better N_2/CH_4 selectivities to/than different types of porous membranes.

MOFs and COFs have a wide range of pore sizes and high porosities that enable their usage as fillers in MMMs to enhance the permeability and selectivity of polymers [90]. Fig. 7 represents $S^0_{mem,\ N_2/CH_4}$ and $P^0_{N_2}$ of 25 different MOF/polymer and 25 different COF/polymer composites consisting of 5 polymers, 5 top MOFs, and 5 top COFs. MOFs and COFs with the highest $S^0_{mem,\ N_2/CH_4}$ were selected as fillers for MMMs. $P^0_{N_2}$ of all MOF/polymer and COF/polymer composites were higher than the corresponding conventional polymeric membranes. Incorporation of MOFs and COFs into the polymers with low $P^0_{N_2}$ (<1000 Barrer) increases the permeability of the polymer without significantly changing $S^0_{mem,\ N_2/CH_4}$. For example, the N_2 permeability of the polymer 6FDA-TAB increased from 2.58 to 4.73 Barrer upon MOF and COF addition while $S^0_{mem,\ N_2/CH_4}$ remained constant at 2.87, which indicates that the improvement in permeability does not depend on the identity of MOFs and COFs. The polymers Hyflon AD 60X, PTMSPcoPP, and Teflon AF 2400 surpassed the upper bound upon the addition of MOFs and COFs, regardless of the identity of MOFs, due to the significant improvements in their permeabilities from 8.3, 153, and 490 Barrer to 15.1, 280, and 894 Barrer, respectively.

Incorporation of MOFs and COFs as fillers into the PTMSP, which

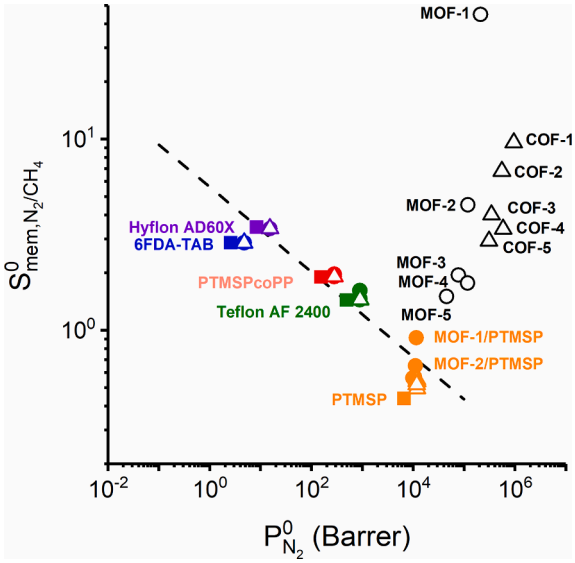


Fig. 7. Performances of the selected MOFs (empty black circles), COFs (empty black triangles) and pure polymers (filled squares) Hyflon AD60X (purple), 6FDA-TAB (blue), PTMSPcoPP(red), Teflon AF 2400 (green), and PTMSP (orange). MOF/polymer (COF/polymer) MMMs are shown with filled circles (empty triangles) in accordance with the colours of the polymers. The dashed line shows the predicted extension of Robeson's upper bound at high N_2 permeabilities. (For interpretation of the references to colour in this Fig. legend, the reader is referred to the web version of this article.)

already have high $P^0_{N_2} > 1000$ Barrer, significantly improved both $P^0_{N_2}$ and $S^0_{mem,\ N_2/CH_4}$. $P^0_{N_2}$ of pure PTMSP increased from 6.6×10^3 Barrer to 9.8×10^3 –1.15×10^4 and 1.16×10^4 –1.19×10^4 Barrer for MOF and COFs, respectively. $S^0_{mem,\ N_2/CH_4}$ of the polymers were improved for all MOF/PTMSP and COF/PTMSP composites; the most significant increase was observed from 0.44 to 0.91 and 0.44 to 0.65 with the addition of UTEWOG and HUYJUG as filler MOFs, respectively. As a result, UTEWOG/PTMSP and HUYJUG/PTMSP composites surpassed the upper bound due to the improvements in both $P^0_{N_2}$ and $S^0_{mem,\ N_2/CH_4}$. However, the other three MOF/PTMSP composites and five COF/PTMSP composites remained close or below the upper bound, suggesting that obtaining MMMs with high selectivity and permeability depends on the proper selection of the polymer and filler. These results indicate incorporating MOFs and COFs into polymers almost doubled N_2 permeabilities and improved N_2/CH_4 selectivities of polymers.

4. Conclusion

In this work, we examined five types of porous materials, MOFs, COFs, IL/MOF composites, MOF/polymer composites, and COF/polymer composites for CH_4/N_2 separation. Comparison of MOFs and COFs revealed that MOFs have higher adsorption selectivities than COFs, but they have comparable APSs at PSA condition. Structure performance relation analysis revealed that the top MOFs have narrow pores, LCD < 10 Å, and low porosities, <0.75, but the top COFs have a wider range of LCDs and porosities, up to 27 Å and 0.85, respectively. We incorporated an IL into the top MOFs to examine the change in adsorption selectivities and analysed the interactions between CH_4, N_2, IL, and MOF by performing DFT calculations. Incorporating an IL further improved selectivities of the top MOFs, which shows the great potential of IL/MOF composites for CH_4/N_2 separation. DFT calculations demonstrated that CH_4 and N_2 primarily interact with the heterocyclic linkers, indicating the importance of linker selection for effective CH_4 adsorption. A large number of MOF and COF membranes surpassed Robeson's upper bound due to high N_2 permeabilities, 1.06×10^4 –2.36×10^6 Barrer,

outperforming conventional polymers. Membrane properties of MOF/polymer and COF/polymer composites were also predicted, and results demonstrated that the use of MOFs and COFs as fillers significantly increased the N_2 permeabilities of all polymers and membrane selectivities of some polymers. Overall, MOFs, COFs, and their composites with ILs and polymers have a remarkable potential for CH_4/N_2 separation compared to traditional materials. By narrowing down the number of potential adsorbent and membrane candidates via high-throughput computational screening and identifying the structural and chemical properties of the top materials, our work will guide future studies for the design of new materials having high CH_4/N_2 separation performances.

Declaration of Competing Interest

The authors declare that they have no known competing financial interests or personal relationships that could have appeared to influence the work reported in this paper.

Acknowledgements

S.K. acknowledges ERC-2017-Starting Grant. This study has received funding from the European Research Council (ERC) under the European Union's Horizon 2020 research and innovation programme (ERC-2017-Starting Grant, grant agreement No 756489-COSMOS).

Appendix A. Supplementary data

Relationship between S^0_{ads} and $S_{ads,\,mix}$ of MOFs and COFs; LCD/PLD ratios and porosities of MOFs and COFs as a function of $S_{ads,\,mix}$; 3D representations of SAHYAD03 cluster model containing the metal center and in the presence of CH_4 and N_2 gases; potential parameters used to describe CH_4 and N_2; Performance metrics to evaluate MOF and COF adsorbents and membranes; experimental single-component gas permeability and selectivity data of polymers; separation performances of the top 20 MOFs and COFs for VSA and PSA and top 5 MOF and COF membranes for CH_4/N_2 and N_2/CH_4 mixture; structures of the selected MOFs, COFs, and IL/MOF composites; Cartesian coordinates of SAHYAD03 model and CH_4, SAHYAD03 model and N_2, SAHYAD03 linker model and CH_4 (Central Triazole Ring), SAHYAD03 linker model and N_2 (Central Triazole Ring), SAHYAD03 linker model and CH_4 (Phenyl and Pyridine Rings), SAHYAD03 linker model and N_2 (Phenyl and Pyridine Rings), [BMIM][SCN], [BMIM][SCN] and CH_4, [BMIM][SCN] and N_2, [BMIM][SCN] and SAHYAD03 linker model. Supplementary data to this article can be found online at https://doi.org/10.1016/j.cej.2021.131239.

References

[1] O.K. Farha, I. Eryazici, N.C. Jeong, B.G. Hauser, C.E. Wilmer, A.A. Sarjeant, R. Q. Snurr, S.T. Nguyen, A.O. Yazaydın, J.T. Hupp, J. Am. Chem. Soc. 134 (2012) 15016–15021.
[2] H. Furukawa, K.E. Cordova, M. O'Keeffe, O.M. Yaghi, Science 341 (2013).
[3] The Cambridge Structural Database (CSD), UK. Available from: https://www.ccdc.cam.ac.uk/CCDCStats/Stats, 2020 (Accessed December 2020).
[4] C. Altintas, S. Keskin, ACS Sustain. Chem. Eng. 7 (2018) 2739–2750.
[5] J. Rogacka, A. Seremak, A. Luna-Triguero, F. Formalik, I. Matito-Martos, L. Firlej, S. Calero, B. Kuchta, Chem. Eng. J. 403 (2021) 126392.
[6] H. Daglar, S. Keskin, J. Phys. Chem. C 122 (2018) 17347–17357.
[7] G. Avci, S. Velioglu, S. Keskin, ACS Appl. Mater. Interfaces 10 (2018) 33693–33706.
[8] R.T. Yang, Adsorbents: fundamentals and applications, John Wiley & Sons, 2003.
[9] G. Sethia, R.S. Somani, H.C. Bajaj, Ind. Eng. Chem. Res. 53 (2014) 6807–6814.
[10] N.K. Jensen, T.E. Rufford, G. Watson, D.K. Zhang, K.I. Chan, E.F. May, J. Chem. Eng. Data 57 (2012) 106–113.
[11] B. Yuan, X. Wu, Y. Chen, J. Huang, H. Luo, S. Deng, Environ. Sci. Technol. 47 (2013) 5474–5480.
[12] Y.-J. Wu, Y. Yang, X.-M. Kong, P. Li, J.-G. Yu, A.M. Ribeiro, A.E. Rodrigues, J. Chem. Eng. Data 60 (2015) 2684–2693.
[13] B. Liu, B. Smit, Langmuir 25 (2009) 5918–5926.
[14] B. Liu, B. Smit, J. Phys. Chem. C 114 (2010) 8515–8522.
[15] Z. Sumer, S. Keskin, Ind. Eng. Chem. Res. 56 (2017) 8713–8722.
[16] T. Yan, Y. Lan, D. Liu, Q. Yang, C. Zhong, Chem. Asian J. 14 (2019) 3688–3693.
[17] Z. Qiao, C. Peng, J. Zhou, J. Jiang, J. Mater. Chem. A 4 (2016) 15904–15912.
[18] Z. Qiao, Q. Xu, J. Jiang, J. Membr. Sci. 551 (2018) 47–54.
[19] O.F. Altundal, C. Altintas, S. Keskin, J. Mater. Chem. A 8 (2020) 14609–14623.
[20] G.O. Aksu, H. Daglar, C. Altintas, S. Keskin, J. Phys. Chem. C 124 (2020) 22577–22590.
[21] J.M. Vicent-Luna, J.J. Gutiérrez-Sevillano, S. Hamad, J. Anta, S. Calero, ACS Appl. Mater. Interfaces 10 (2018) 29694–29704.
[22] H.M. Polat, M. Zeeshan, A. Uzun, S. Keskin, Chem. Eng. J. 373 (2019) 1179–1189.
[23] Y.G. Chung, E. Haldoupis, B.J. Bucior, M. Haranczyk, S. Lee, H. Zhang, K. D. Vogiatzis, M. Milisavljevic, S. Ling, J.S. Camp, J. Chem. Eng. Data 64 (2019) 5985–5998.
[24] T. Yan, Y. Lan, M. Tong, C. Zhong, ACS Sustain. Chem. Eng. 7 (2018) 1220–1227.
[25] D. Ongari, A.V. Yakutovich, L. Talirz, B. Smit, ACS Cent. Sci. 5 (2019) 1663–1675.
[26] T.F. Willems, C.H. Rycroft, M. Kazi, J.C. Meza, M. Haranczyk, Microporous Mesoporous Mater. 149 (2012) 134–141.
[27] K.B. Sezginel, A. Uzun, S. Keskin, Chem. Eng. Sci. 124 (2015) 125–134.
[28] D. Dubbeldam, S. Calero, D.E. Ellis, R.Q. Snurr, Mol. Simul. 42 (2016) 81–101.
[29] A.K. Rappé, C.J. Casewit, K. Colwell, W.A. Goddard III, W.M. Skiff, J. Am. Chem. Soc. 114 (1992) 10024–10035.
[30] M.G. Martin, J.I. Siepmann, J. Phys. Chem. B 102 (1998) 2569–2577.
[31] K. Makrodimitris, G.K. Papadopoulos, D.N. Theodorou, J. Phys. Chem. B 105 (2001) 777–788.
[32] A.K. Rappe, W.A. Goddard III, J. Phys. Chem. A 95 (1991) 3358–3363.
[33] C.E. Wilmer, R.Q. Snurr, Chem. Eng. J. 171 (2011) 775–781.
[34] P.P. Ewald, Annalen der physik 369 (1921) 253–287.
[35] T. Vlugt, E. García-Pérez, D. Dubbeldam, S. Ban, S. Calero, J. Chem. Theory Comput. 4 (2008) 1107–1118.
[36] M. Zeeshan, S. Keskin, A. Uzun, Polyhedron 155 (2018) 485–492.
[37] F.P. Kinik, C. Altintas, V. Balci, B. Koyuturk, A. Uzun, S. Keskin, ACS Appl. Mater. Interfaces 8 (2016) 30992–31005.
[38] B. Koyuturk, C. Altintas, F.P. Kinik, S. Keskin, A. Uzun, J. Phys. Chem. C 121 (2017) 10370–10381.
[39] H.M. Polat, S. Kavak, H. Kulak, A. Uzun, S. Keskin, Chem. Eng. J. 394 (2020), 124916.
[40] Ö. Durak, H. Kulak, S. Kavak, H.M. Polat, S. Keskin, A. Uzun, J. Phys. Condens. Matter 32 (2020), 484001.
[41] M. Zeeshan, H. Kulak, S. Kavak, H.M. Polat, O. Durak, S. Keskin, A. Uzun, Microporous Mesoporous Mater. 306 (2020), 110446.
[42] A.D. Becke, J. Chem. Phys. 98 (1993) 5648–5652.
[43] C. Lee, W. Yang, R.G. Parr, Phys. Rev. B 37 (1988) 785–789.
[44] S. Grimme, J. Antony, S. Ehrlich, H. Krieg, J. Chem. Phys. 132 (2010), 154104.
[45] E. Adatoz, S. Keskin, J. Nanomater. 2015 (2015).
[46] D.J. Evans, B.L. Holian, J. Chem. Phys. 83 (1985) 4069–4074.
[47] D. Dubbeldam, D.C. Ford, D.E. Ellis, R.Q. Snurr, Mol. Simul. 35 (2009) 1084–1097.
[48] V. Colombo, S. Galli, H.J. Choi, G.D. Han, A. Maspero, G. Palmisano, N. Masciocchi, J.R. Long, Chem. Sci. 2 (2011) 1311–1319.
[49] T. Prior, M. Rosseinsky, Inorg. Chem. 42 (2003) 1564–1575.
[50] M. Tonigold, D. Volkmer, Inorganica Chim. Acta 363 (2010) 4220–4229.
[51] X.Z. Xi-Hui Liu, Chao Liu, Tai-Zhu Liu, Wuji Huaxue Xuebao, 30 (2014) 1128.
[52] K.J. Gagnon, S.J. Teat, Z.J. Beal, A.M. Embry, M.E. Strayer, A. Clearfield, Cryst. Growth Des. 14 (2014) 3612–3622.
[53] Y. Du, H. Yang, J.M. Whiteley, S. Wan, Y. Jin, S.H. Lee, W. Zhang, Angew. Chem. Int. Ed. 128 (2016) 1769–1773.
[54] C. Wang, Y. Wang, R. Ge, X. Song, X. Xing, Q. Jiang, H. Lu, C. Hao, X. Guo, Y. Gao, Chem. Eur. J. 24 (2018) 585–589.
[55] F.J. Uribe-Romo, C.J. Doonan, H. Furukawa, K. Oisaki, O.M. Yaghi, J. Am. Chem. Soc. 133 (2011) 11478–11481.
[56] S. Zhao, B. Dong, R. Ge, C. Wang, X. Song, W. Ma, Y. Wang, C. Hao, X. Guo, Y. Gao, RSC Adv. 6 (2016) 38774–38781.
[57] L.M. Robeson, J. Membr. Sci. 320 (2008) 390–400.
[58] R.L. Burns, W.J. Koros, Macromolecules 36 (2003) 2374–2381.
[59] M. Macchione, J.C. Jansen, G. De Luca, E. Tocci, M. Longeri, E. Drioli, Polym. J. 48 (2007) 2619–2635.
[60] K. Nagai, A. Higuchi, T. Nakagawa, J. Polym. Sci. Part B Polym. Phys. 33 (1995) 289–298.
[61] T. Merkel, V. Bondar, K. Nagai, B. Freeman, J. Polym. Sci. Part B Polym. Phys. 38 (2000) 273–296.
[62] T. Merkel, V. Bondar, K. Nagai, B. Freeman, Y.P. Yampolskii, Macromolecules 32 (1999) 8427–8440.
[63] J. Maxwell, A treatise on Electricity and Magnetism, Dover, 1954.
[64] R. Bouma, A. Checchetti, G. Chidichimo, E. Drioli, J. Membr. Sci. 128 (1997) 141–149.

[65] S. Budhathoki, O. Ajayi, J.A. Steckel, C.E. Wilmer, Energy Environ. Sci. 12 (2019) 1255–1264.
[66] H. Daglar, I. Erucar, S. Keskin, J. Membr. Sci. 618 (2021), 118555.
[67] I. Derycke, J.-P. Vigneron, P. Lambin, A. Lucas, E. Derouane, J. Chem. Phys. 94 (1991) 4620–4627.
[68] E.J. Garcia, J. Pérez-Pellitero, G.D. Pirngruber, C. Jallut, M. Palomino, F. Rey, S. Valencia, Ind. Eng. Chem. Res. 53 (2014) 9860–9874.
[69] Y.S. Bae, R.Q. Snurr, Angew. Chem. Int. Ed. 50 (2011) 11586–11596.
[70] D. Beaudoin, T. Maris, J.D. Wuest, Nat. Chem. 5 (2013) 830–834.
[71] Q. Gao, X. Li, G.-H. Ning, H.-S. Xu, C. Liu, B. Tian, W. Tang, K.P. Loh, Chem. Mater. 30 (2018) 1762–1768.
[72] B. Liu, Q. Yang, C. Xue, C. Zhong, B. Chen, B. Smit, J. Phys. Chem. C 112 (2008) 9854–9860.
[73] Y. Basdogan, K.B. Sezginel, S. Keskin, Ind. Eng. Chem. Res. 54 (2015) 8479–8491.
[74] A. Henley, M.J. Lennox, T.L. Easun, F. Moreau, M. Schröder, E. Besley, J. Phys. Chem. C 120 (2016) 27342–27348.
[75] M. Chang, J. Ren, Q. Yang, D. Liu, Chem. Eng. J. (2020), 127294.
[76] Q.-K. Liu, J.-P. Ma, Y.-B. Dong, ChemComm 47 (2011) 12343–12345.
[77] R. Haldar, T.K. Maji, J. Chem. Sci. 123 (2011) 883–890.
[78] Z. Xu, L.L. Han, G.L. Zhuang, J. Bai, D. Sun, Inorg. Chem. 54 (2015) 4737–4743.
[79] X. Wu, B. Yuan, Z. Bao, S. Deng, J. Colloid Interface Sci. 430 (2014) 78–84.
[80] Z. Niu, X. Cui, T. Pham, P.C. Lan, H. Xing, K.A. Forrest, L. Wojtas, B. Space, S. Ma, Angew. Chem. Int. Ed. 58 (2019) 10138–10141.
[81] M. Chang, J. Ren, Q. Yang, D. Liu, Chem. Eng. J. 408 (2021), 127294.
[82] L. Li, L. Yang, J. Wang, Z. Zhang, Q. Yang, Y. Yang, Q. Ren, Z. Bao, AlChE J. 64 (2018) 3681–3689.
[83] M. Chang, Y. Zhao, D. Liu, J. Yang, J. Li, C. Zhong, Sustain. Energy Fuels 4 (2020) 138–142.
[84] A.M. Mohamed, S. Moncho, P. Krokidas, K. Kakosimos, E.N. Brothers, I. G. Economou, Mol. Phys. 117 (2019) 3791–3805.
[85] B.D. Freeman, Macromolecules 32 (1999) 375–380.
[86] X. Ning, W.J. Koros, Carbon 66 (2014) 511–522.
[87] Y. Huang, L. Wang, Z. Song, S. Li, M. Yu, Angew. Chem. Int. Ed. 127 (2015) 10993–10997.
[88] Z. Zong, S.K. Elsaidi, P.K. Thallapally, M.A. Carreon, Ind. Eng. Chem. Res. 56 (2017) 4113–4118.
[89] S. Wu, X. Li, B. Liu, B. Wang, R. Zhou, Energy Fuels (2020).
[90] J. Dechnik, J. Gascon, C.J. Doonan, C. Janiak, C.J. Sumby, Angew. Chem. Int. Ed. 56 (2017) 9292–9310.